COMPRESSION BEHAVIOR OF LATTICE STRUCTURES PRODUCED BY SELECTIVE LASER MELTING: X-RAY TOMOGRAPHY BASED EXPERIMENTAL AND FINITE ELEMENT APPROACHES

Yasin Amani[a], Sylvain Dancette[a,*], Pauline Delroisse[b], Aude Simar[b], Eric Maire[a]

[a] *INSA de Lyon, MATEIS CNRS UMR5510, Université de Lyon, 69621 Villeurbanne, France*
[b] *Institute of Mechanics, Materials and Civil Engineering (iMMC), Louvain-La-Neuve, Belgium*

Abstract

The compression behavior of hollow architectured structures obtained by additive manufacturing was investigated in this work. Two face-centered cubic structures with the same shape and repetitive pattern but different struts and nodes thicknesses were produced using the selective laser melting (SLM) technique. Deformation of the structures under compression was imaged by in-situ and ex-situ X-ray tomography scanning. The initial state of the structure was scanned using the stitching tomography method to capture detailed 3D images illustrating both the macroscopic hollow structure and local microporosity in the nodes and struts. A 3D image-based conformal finite element model was then built for the simulation of the compression test using Gurson-Tvergaard-Needleman (GTN) porous plasticity and a new procedure allowing to inform the local porosity of each element directly from high resolution tomography. Simulations considering a homogeneous matrix with an average initial porosity everywhere were compared to the new heterogeneous model. A fairly good agreement was found between the heterogeneous model and experiments espe-

*Corresponding author. Tel.: +33 (0) 47 243 8541
Email address: sylvain.dancette@insa-lyon.fr (Sylvain Dancette)

cially in the prediction of fracture location.

Keywords: Additive Manufacturing, Aluminum lattice, Ductile fracture, 3D image analysis, Finite element modeling

---

1. Introduction

Additive Manufacturing (AM) is a new concept to manufacture a cellular structure with high levels of complexity from pre-alloyed, atomized precursor powders. A 3D model designed by a computer-aided design (CAD) software is described by 2D slices with a given layer thickness. Layers are built up subsequently by adding materials [1]. Selective Laser Melting (SLM) is a class of AM techniques where a laser source selectively melts layers of metal powder particles forming a near-net-shape structure according to a 3D CAD model [2, 3, 4, 5]. The time at high temperature in each part of the sample depends on its corresponding local thickness, which will inevitably affect the coarseness of the microstructure [6]. The mechanical properties of a cellular structure processed by SLM may be better than processed by a casting route [4].

Non-destructive X-ray tomography provides a 3D vision into the microstructure and internal defects of the cellular structure. 2D and 3D images with low resolution have been used to determine the morphological characteristics (3D architecture, cell size, shape fraction of solid in the edges, cell connectivity, sphericity and tortuosity) of the cellular structure [7, 8, 9, 10, 11]. However, in order to inspect the internal defects of their solid phase, high resolution 3D images are required [6]. The deformation chronology of cellular structures has been tackled by performing in-situ/ex-situ compression tests coupled with X-ray tomography scanning [12, 13, 14, 15, 16, 17, 18]. Moreover, with the recent progresses in 3D image processing and meshing procedures in the last two decades, numerous studies used the Finite Element (FE) method to further analyze the behavior of cellular structures by direct conversion of the 3D tomographic images to FE meshes [19, 20, 21, 22, 23, 24, 25, 26, 27, 28, 29, 30, 31, 32, 17, 33, 34, 18, 35]. Youssef et al. [19] and Caty et al. [22] developed one of the first and most

efficient method to obtain a FE mesh representing a cellular material. Using a similar FE procedure, Zhang et al. [36] anticipated fracture in the material based on the contour plot of von Mises stress after simulation. Petit et al. [35] extended this method by running FE simulations and qualitatively defining elastoplastic and damage properties for the aluminium and intermetallic particles in an attempt to account for the latter in the prediction of mechanical behavior. Next to these 3D image-based FE elements studies of porous structures, several idealized 2D models have been proposed in the last decade to predict their deformation and fracture behavior [37, 38, 39, 40].

As concerns regular AM lattice structures, Challis et. al. developed CAD based FE models of the unit cells of two 3D lattices for predicting their Young's moduli and strengths [41]. Several attempts were performed to predict the compressive responses compared to the experiments by performing CAD based FE calculation of the lattice structures [42, 43, 44]. Karamooz et. al. developed a CAD-based FE model of a 3D lattice including both constant and variable cross section from the probability of the diameters of the struts. It had been shown that the FE model accounting for cross-section variations along the strut's length predicts a lower mechanical stress-strain curve compared to the model with constant cross-section [45].

The walls/beams of metallic cellular or AM structures may contain significant amount of microporosity, as documented for example in [20, 46]. Some studies [20, 30] tried to take the presence of such microporosity into account in the FE simulation of the foam behavior, using an explicit meshing procedure of both macroscopic void-cells and local microcavities. Such full-field approach of image-based void evolution during deformation has also been investigated within the framework of ductile damage studies (e.g. [47, 48, 49]). This becomes however intractable for large sample meshes and huge number of microcavities, which would require several millions of finite elements and unaffordable computer ressources and computation time. A common alternative to model the effect of voids on mechanical behavior in an average sense consists in the use

of Gurson-type continuum models such as the Gurson-Tvergaard-Needleman (GTN) model [50]. The parameters of the GTN model can be adjusted to some extent to match 3D experimentally measured void-growth kinetics [51] or crack propagation [52]. However, multiscale microstructure-informed modeling of ductile damage in real size materials or structures remains a challenge [49]. This applies also to cellular or macroporous materials. To the authors' knowledge, no study has yet been performed to both quantify and model the effect of macroscopic void-cell fraction combined with the local microporosity level on the mechanical behavior of real macroporous structures, with a statistically representative size.

The present paper focuses on the characterization of Face Centered Cubic (FCC) lattice structures at two resolutions. They were produced with identical solid skeleton but different strut and node thicknesses. The porosity level was characterized using local tomography and double detector techniques simultaneously. Subsequently, displacement stepped in-situ/ex-situ compression tests were coupled with low-resolution X-ray tomography scanning to track the progressive fracture of the samples. Fracture could then be linked with its initial morphological features. Finally, a new procedure was developed to build FE models directly based on the detailed 3D images and informed by the local microporosity level in the struts. FE simulations of the compression tests could then be run with a GTN model informed by the local porosity level in each element of the nodes and struts (heterogeneous model) and compared to the corresponding simulations with average initial porosity (homogeneous model). The new procedure allows to investigate the effect of local heterogeneous microporosity on mechanical behavior without significant increase of the requirement in computer resources and can be transfered easily to any type of problem where local, image-based microstructural heterogeneity might affect the damage behavior.

2. Materials and experiments

Two FCC samples produced by SLM with different thicknesses [6] were characterized in this study. The samples were manufactured with AlSi10Mg powders. The processing parameters of the SLM 250 equipment were a laser power of 250 W, a scanning speed of 571 mm/s, a layer thickness of 60 μm and an argon gas atmosphere. The mechanical properties of the bulk structure produced are provided in Table 1 [5]. It shows that changing the build direction affects insignificantly the plastic properties but the maximum load and corresponding elongation are slightly lower in the vertical direction i.e. the building direction. The dimensions of both samples were a 20.0 mm side cube. Both samples contained five cells in x, y and z directions. y is the building direction and the two horizontal directions are x and z, respectively.

Table 1: Mechanical properties of the bulk specimens fabricated in the vertical (SLM building direction) and horizontal directions [5].

Test direction	Young's modulus (GPa)	Yield strength (MPa)	Ultimate tensile strength (UTS) (MPa)	Elongation at UTS (%)
Vertical	70.7±4.7	169±5	273±10	8.2±1.2
Horizontal	70.2±4.9	169±4	267±10	9.1±1.9

2.1. "Double detector" tomography technique

X-ray tomography scanning with two different scales was performed to capture the architecture and internal defects of the samples. X-ray computed tomography is based on X-ray radiography. The result of which is a 2D image of a 3D object projected on the detector screen. The detector had 1920 × 1536 square sensitive pixels. By using low-resolution scanning (here 20 μm pixel size), the entire geometry of the samples was fully visible in the field of view (FOV) of the detector allowing to capture the entire architecture of the 5x5 cellular structure. However, by using this resolution, the internal cavities smaller than 60 μm could not be observed by the detector (Figures 1(a) and (c)). Therefore, another method called "double detector" or "stitching" tomography technique was used coupling with local tomography at a pixel size of 8 μm. In this method,

the field of view of the detector was expanded horizontally by moving the detector while the local tomography scanning was performed. Vertical portions of the specimen were placed step by step in the FOV during rotation. 3D images with a 8 μm voxel size could thus be obtained as illustrated in Figures 1(b) and (d). Figure 2 illustrates a local view of the thin-strut samples. Cavities are represented in red. Cavities with bigger size in the node and smaller size along the struts are clearly visible. The larger cavities are expectedly lack of fusion defects due to the scanning strategy. The smaller cavities are due to degassed and trapped hydrogen and/or argon bubbles during the manufacturing process [6]. It will be shown in section 4 that the lack of fusion defects are not responsible for the sample failure. Figures 3(a) and (b) illustrate the 3D microstructures of the thin-strut and thick-strut samples containing cavities, as obtained with the Avizo software [53].

During each scan, the sample was rotated in 2500 steps between 0 ° and 360 ° and an average of three images were taken at each step. Then, a standard filtered back-projection algorithm was used to reconstruct the final 3D image. The X-ray tube operated at an acceleration voltage of 90 kV using a tungsten transmission target with a 280 μA current. The spot size was 3 μm during all scans i.e. sufficiently lower than the pixel size to prevent any geometrical blur.

2.2. Morphological parameters

The detailed 3D tomographic images were analyzed using the Fiji software [54] to evaluate morphological characteristics of the microstructure such as node, strut and void-cell thicknesses. First, the 3D tomographic images of the struts (including their internal cavities) were segmented as white color and large voids of the cellular structure as black. Then, the white voxels were analyzed by a plugin of the Fiji program computing the local thickness of the 3D structure. The plugin estimates the local thickness by the largest sphere that fits inside the solid phase and contains its voxels. The result of the analysis is a 3D stack of the foam structure with different colors corresponding to different local thicknesses

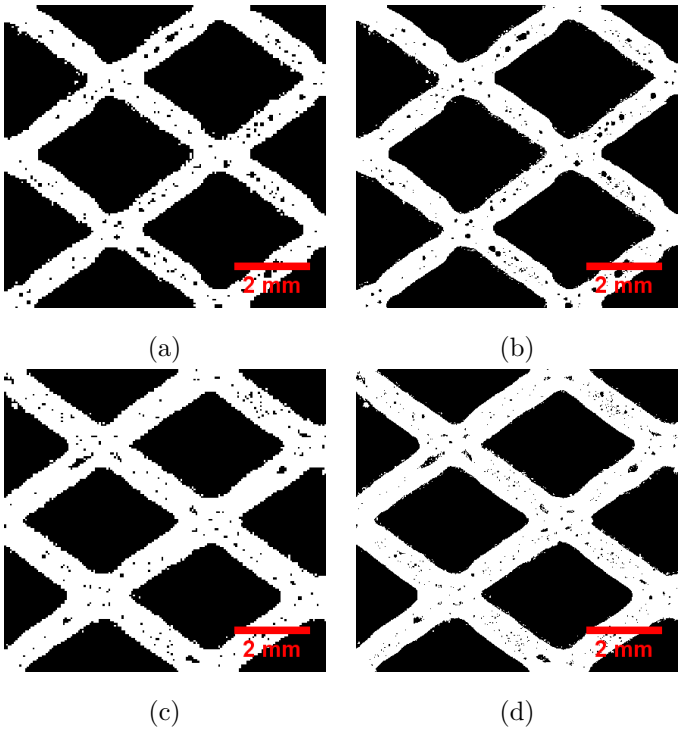


Figure 1: One diagonal slice of the 3D tomographic image of the FCC structure (initial state) with either thin struts (a and b) or thick struts (c and d) at either 20 μm (a and c) or 8 μm (b and d) voxel size.

[55]. The average node and strut diameters are listed in Table 2. The histogram of the number of voxels presenting a given local thickness has two peaks which correspond to the average strut diameter and the average node diameter (Figure 4). The two curves have peaks at low thickness values corresponding to partially melted powder particles attached to the surface of the struts.

Table 2: Morphological characteristics of the two types of FCC structures as computed with the local thickness algorithm.

Parameter	Thin-strut	Thick-strut
Node diameter (mm)	1.02 $\pm$ 0.19	1.13 $\pm$ 0.14
Strut diameter (mm)	0.66 $\pm$ 0.56	0.79 $\pm$ 0.59

Thickness distributions of the samples were determined in x, y and z di-

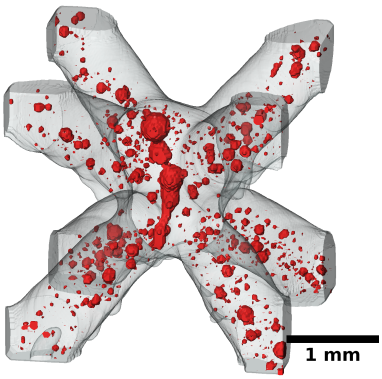
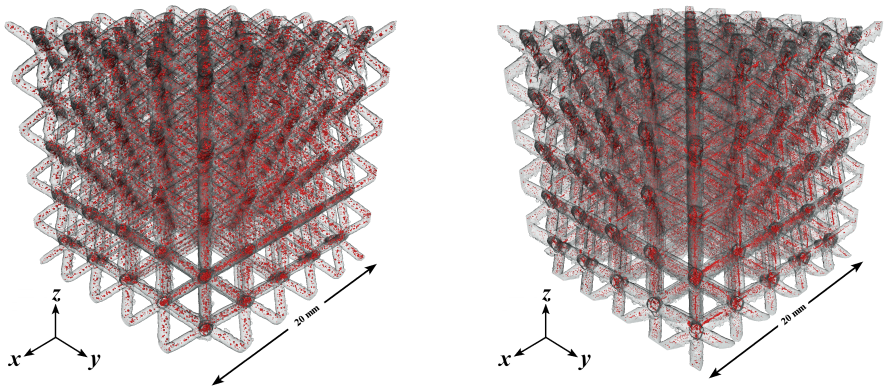


Figure 2: Local cavities in red and AlSi10Mg phase in transparent gray in a node and struts of the thin-strut sample in the initial state.

rections using a home-made plugin of the Fiji program. The plugin counts the number of intercepts passing through the voxels of the solid phase segmented in white. Figures 5(a) and (b) illustrate the thickness distributions of the samples in x, y and z directions. It shows clearly that the average strut thicknesses of both samples in the y direction is higher than in the x and z directions.

In order to evaluate the geometrical characteristics of the cavities in the solid phase of the samples, the 8 μm voxel size 3D images were segmented in black, grey and white colors corresponding to macroscopic void-cells of the lattice structure, AlSi10Mg and microcavities. The volume fraction of each phase in the 3D stack is listed in Table 3. The overall microporosity values of the thin-strut and the thick-strut samples were evaluated as $f_0 = 2.01\,\%$ and $f_0 = 1.12\,\%$ respectively. These values are consistent with the even higher resolution X-ray tomography image analysis (1.5 μm voxel size) performed by Delroisse *et al.* [6] on the struts of the thin-strut sample. They found microporosity values ranging from 0.1 % (classical in bulk SLM samples) to 3.7 % in the bottom of the struts due to differences in the cooling conditions.

Each cluster of connected white voxels was labeled and then analyzed by a second home-made plugin. It evaluated the Feret diameters of each seg-



(a) (b)

Figure 3: Internal cavities (in red) and AlSi10Mg phase (in transparent gray) in the initial state of (a) thin struts and (b) thick struts FCC structure.

Table 3: Volume fractions of macroscopic void-cells and microcavities with respect to the entire $20 \times 20 \times 20$ mm^3 volumes.

Morphology	Void-cells (%)	Microcavities (%)
Thin-strut	83.37	2.01
Thick-strut	77.32	1.12

mented phase from the maximum and minimum x, y and z values, as well as the sphericity. The resulting geometrical characteristics are listed in Table 4. The contribution of small ($< 31\,\mu$m) and large ($> 31\,\mu$m) microcavities to the global microporosity is listed in Table 5. It shows that most of the microporosity in volume fraction arises from the larger microcavities with an average size above $31\,\mu$m for both thin-strut and thick-strut samples.

Table 4: Geometrical characteristics of microcavities in the solid phase. The minimum and maximum values registered are provided under parenthesis.

Parameter	Thin-strut	Thick-strut
Feret diameter in x (μm)	38 (24 $\sim$ 978)	36 (24 $\sim$ 1722)
Feret diameter in y (μm)	39 (24 $\sim$ 1542)	37 (24 $\sim$ 2022)
Feret diameter in z (μm)	38 (24 $\sim$ 1038)	35 (24 $\sim$ 2040)
Sphericity (-)	0.83 ± 0.17	0.83 ± 0.20

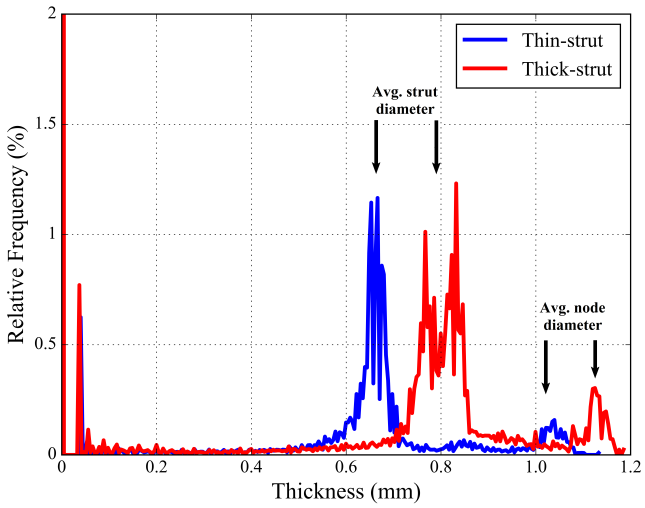


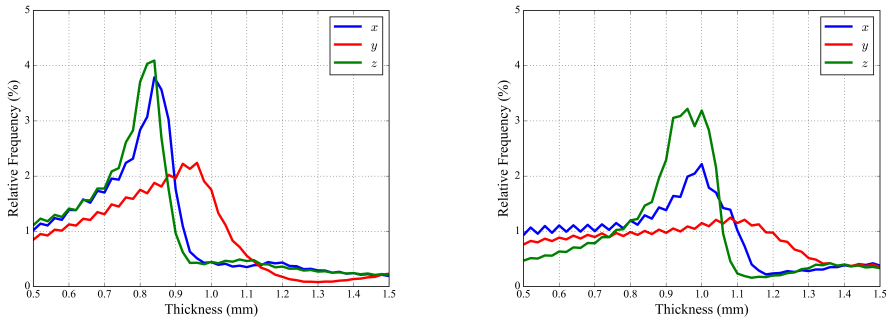
Figure 4: Local thickness distributions of the two FCC structures in the initial state.

Table 5: Contributions of the two microporosity families in the struts and nodes of the FCC structures to the global microcavity volume fractions of Table 3.

Morphology	Small microcavities $< 31\,\mu$m (%)	Large microcavities $> 31\,\mu$m (%)
Thin-strut	0.09	1.92
Thick-strut	0.07	1.05

2.3. In-situ/ex-situ compression tests

Plastic deformations of the two samples were observed by performing compression tests coupled with in-situ/ex-situ X-ray tomography scanning. A home-made testing machine described in Buffiere *et al.* [56] with 5 kN load cell was used for the in-situ steps while a universal Instron testing machine was used for ex-situ steps. The maximum load required for the compression test of the thin-strut sample was below the maximum load of the in-situ testing machine. In the case of the thick-strut sample, the maximum load was too large to use the in-situ machine and thus the test was performed ex-situ. Each loading step was performed at a crosshead displacement speed of 0.001 mm/s controlled by a desktop computer storing data sent from the force transducer and the extensometer. Both samples were compressed along the z direction. The crosshead



(a) (b)

Figure 5: Initial thickness distributions of (a) thin-strut and (b) thick strut samples in x, y and z directions.

displacement was stopped after each displacement step. The entire architecture of the deformed sample was scanned at low resolution (20 μm voxel size). The strain values were evaluated considering the position of the top and bottom surfaces of the sample in the 3D tomographic images taken at each deformation step ($\varepsilon_z = \frac{\Delta l}{l_0}$). Stress values were obtained by dividing the measured force by the initial cross-section area of the sample ($\sigma_{zz} = \frac{F}{A_0}$).

3. Finite element model

In this study a standard Gurson-Tvergaard-Needleman (GTN) [57, 58, 59, 60, 50] model is used to represent void nucleation and growth in the simulation within the Abaqus environment. The GTN model is developed based on von Mises yield criteria of ductile porous materials incorporating void nucleation and growth. The governing equations of this model are defined as:

$$\Phi\left(\sigma_{eq}, \sigma_y, \sigma_H, f\right) = \left(\frac{\sigma_{eq}}{\sigma_y}\right)^2 + 2fq_1 \cosh\left(\frac{3q_2\sigma_H}{2\sigma_y}\right) - \left(1 + q_3 f^2\right) = 0 \qquad (1)$$

where Φ is the yield function, q_1, q_2 and q_3 are calibrating parameters, σ_{eq} is the von Mises equivalent stress, σ_y is the yield stress, σ_H is the hydrostatic

stress, and f is the void volume fraction (VVF) in the matrix. In addition, the evolution of f, starting from an initial VVF f_0, is defined as [58]:

$$\dot{f} = \dot{f}_{gr} + \dot{f}_{nucl} = (1-f)\ tr(\dot{\boldsymbol{\varepsilon}}^{pl}) + \frac{f_N}{s_N\sqrt{2\pi}} \exp\left[-\frac{1}{2}\left(\frac{\varepsilon_{eq}^{pl} - \varepsilon_N}{s_N}\right)^2\right] \dot{\varepsilon}_{eq}^{pl} \quad (2)$$

where $\dot{f}_{gr}$ is the void growth rate which is based on mass conservation and directly proportional to the hydrostatic component of the plastic strain rate tensor $\dot{\boldsymbol{\varepsilon}}^{pl}$ and ε_{eq}^{pl} is the equivalent plastic strain. Furthermore, ε_N and s_N are the mean value and standard deviation of the normal nucleation distribution, respectively. f_N is the volume fraction of nucleated voids. The parameters of the GTN model are q_1 =1.5 , q_2 =1.0 and q_3 =2.25 [60]. The power law work hardening used in this study is defined as [61]:

$$\frac{\sigma_y}{\sigma_0} = \left(\frac{\sigma_y}{\sigma_0} + \frac{3G}{\sigma_0}\varepsilon^{pl}\right)^N \quad (3)$$

where σ_y is the current flow stress, σ_0 is the initial yield stress, N is the hardening exponent and G is the elastic shear modulus. In this study, the 3D tomographic images of the initial state of the samples were taken as the geometric description of the model to generate FE meshes. First, a surface mesh was generated, consisting of triangles fitting to the boundary of the solid phase. Then, the surface mesh was simplified to reduce the number of triangles while preserving a good description of the surface. Finally, the solid volume was filled by first-order tetrahedra [19] which is consistent with an Abaqus Explicit analysis. The entire meshing procedure was performed using the commercial software Avizo® [53]. The number of tetrahedra and nodes of the volume meshes generated are provided in Table 6.

Local defects including microcavities and surface roughness may affect the stress distribution. A mesh convergence test was carried out in order to ensure that the selected mesh size in Table 6 provided comparable local stress distribution as the one obtained with a finer mesh (3.6-fold increase in the number of

elements). Such refinement lowers the apparent Young's modulus of the thin-strut sample by 7 % and its apparent yield stress by about 15 %, at the cost of a severe increase in computation time and resources. Table 6 mesh size emerged therefore as a good compromise between geometrical conformity to the original volume, numerical precision of the mechanical fields and calculation time.

Table 6: Characteristics of the generated mesh volumes of the FCC structures.

Morphology	Number of nodes	Number of elements	Average element size (μm)
Thin-strut	227719	832484	300
Thick-strut	301573	1206697	300

FE computations of thin-strut and thick-strut samples were run to study the effect of microporosity on the resulting stress-strain curves and local stress distribution. The FE computations were run considering three different conditions: non porous J2 (isotropic) plasticity, homogeneous GTN model and heterogeneous GTN model. Note that the non porous J2 plasticity model will be referred to as J2 plasticity only in the following for the sake of simplicity.

Material properties given to the tetrahedra are listed in Table 7 and 8 for the isotropic elasto-plastic behavior and the GTN nucleation parameters respectively. They were obtained with the following procedure based on an axisymmetric uniaxial tension model of the bulk AlSi10Mg alloy with the nominal properties listed in Table 1. Starting from the initial nominal yield stress σ_0 of 169 MPa, the hardening exponent N was set to ensure that the onset of necking in tension, following a Considere criterion, occurred at $\varepsilon = 0.08$, the value of uniform elongation at UTS. In the GTN nucleation model, $f_N = 0.04$ was fixed following the recommended value for ductile aluminum media [35]. ε_N and s_N were adjusted so that the maximum engineering stress was reached at an engineering strain of 0.08 and failure happened at an engineering strain of 0.18 for a material with an initial porosity $f_0 = 0$, with the constraint of $s_N \leq \frac{\varepsilon_N}{3}$ to prevent void nucleation before the initiation of plasticity.

The hardening and damage nucleation parameters being identified on the

bulk material, adjustments of the initial yield stress σ_0 had to be performed for the thin-strut and thick-strut structures (Table 7) in order to retrieve their respective apparent yield strength values. Indeed, the microstructure induced during the fabrication of thin (strut-like) structures may be different from the one obtained in the bulk material as discussed in [6]. This is related especially to the cooling rate experienced locally during solidification, which depends on the local thickness of the material being produced. Moreover, significant surface roughness of the lattice struts might have two consequences on the behavior of the lattice structure: (i) the effective load-bearing cross-section of the struts is lower than the outer envelope of the struts and (ii) the friction between the sample and the two compression plates is higher, resulting in an increased constraint of the sample deformation during the tests. Consequently, the higher surface roughness of the thick-strut sample might explain the need for a higher adjustment of its initial yield stress to $\sigma_0 = 220\,\mathrm{MPa}$ in Table 7.

Table 7: Material properties assigned to the FE computation of the FCC structures.

Morphology	Young's modulus E (GPa)	Poisson ratio ν	Initial true yield stress σ_0 (MPa)	Hardening exponent N	Density ρ ($\mathrm{kg{\cdot}m^{-3}}$)
Thin-strut	70	0.33	160	0.084	2700
Thick-strut	70	0.33	220	0.084	2700

Table 8: The best-fitted GTN model nucleation parameters for the FE computation of the FCC structures.

Mean ε_N	Standard deviation s_N	Volume fraction f_N
0.18	0.06	0.04

In order to build the *heterogeneous* FE model, a python script was developed to inform each finite element with the local initial microporosity level, f_0. The code compares the coordinates of the cavities in the $8\,\mu$m voxel size tomography scans with the coordinates of the tetrahedra in the image-based finite element meshes. The porosity of a tetrahedron is defined based on the number of white (i.e. porosity) voxels whose x, y, z coordinates are located in the tetrahedron interior. Afterwards, all the tetrahedra were sorted into 100 classes corresponding

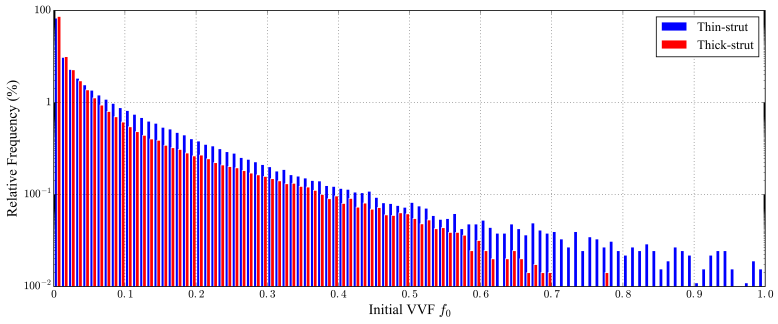


Figure 6: Initial porosity distributions in the tetrahedra evaluated for the volume meshes of the thin-strut and thick-strut samples.

to 100 equally spaced porosity values ranging from 0 to 0.99. The distribution of porosity or so-called "initial Void Volume Fraction" (f_0) in the tetrahedra of the thin-strut and thick-strut samples are illustrated in Figure 6. In contrast to the *heterogeneous* model, the computation of the *homogeneous* GTN model was conducted by assigning the homogeneous average initial VVF value of $f_0 = 0.02$ (thin-strut) and $f_0 = 0.01$ (thick-strut) to all the elements, with the same hardening and damage parameters of Tables 7 and 8.

Figure 7 shows stress-strain curves resulting from computations of the 2D axisymmetric model with a variation of f_0 between 0 and 0.08. It shows clearly that the UTS and the strain at UTS decrease with increasing porosity. It should be noted that the GTN model is applicable for initial VVF (f_0) lower than 0.1. The GTN model overestimates the stress for finite elements with an initial VVF between 0.1 and 0.6. The load bearing capacity of finite elements with an initial VVF larger than 0.6 is equal to zero. In the present study, the relative frequency of tetrahedra with a VVF between 0.1 and 0.99 is below 1 %, resulting in a low effect on the overall stress-strain behavior of the cellular structures.

The FE approach adopted here is a uniaxial monotonous compression loading on the generated homogeneous and heterogeneous volume meshes. Figure 8 shows the typical boundary conditions imposed on the mesh of the thick-strut

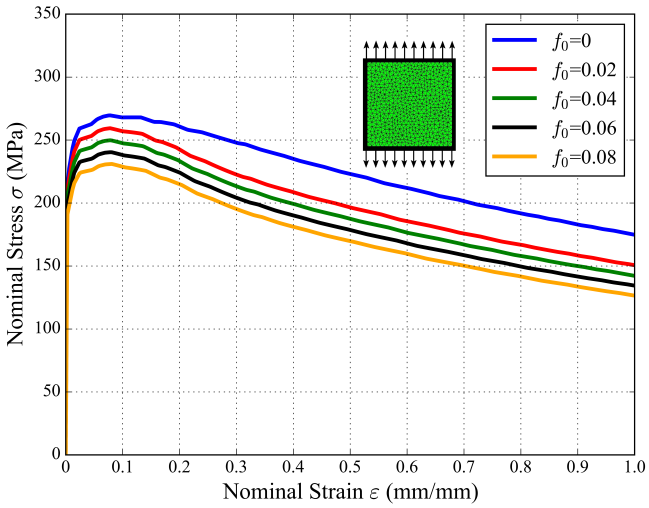


Figure 7: Stress-strain curves of aluminum based materials with the variation of the initial VVF (f_0) obtained by 2D axisymmetric simulations for strain up to $\varepsilon = 1.0$.

sample. Two nodes, one on the top and another on the bottom surfaces of the samples were assigned as master nodes. z displacement degree of freedom of all nodes located on the top surface was constrained to be the same as the z displacement of the top master node, which was subjected to an imposed displacement of 1.5 mm. Similarly, z degree of freedom of the bottom master node was blocked and it was coupled to all other nodes on the bottom surface. Furthermore, nodes located on two central lines, one on the top and another on the bottom surface (blue lines in Figure 8), were blocked in the x direction to prevent global rotation about the compression axis. Identical boundary conditions were imposed on the model of the thin-strut sample.

4. Results and discussion

The predicted stress-strain curves of the non porous J2 plasticity, homogeneous and heterogeneous GTN model are compared to the experimental curves in Figures 9(a) and (b) for the thin-strut and thick-strut samples respectively.

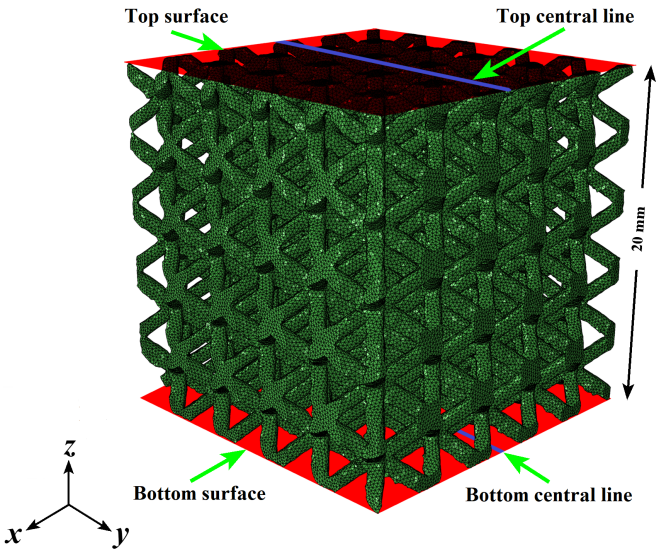


Figure 8: Boundary conditions imposed on the volume mesh of the thick-strut sample.

It is clear that the FE simulations based on J2 plasticity result in overestimated stress values compared to experiments. The presence of microcavities in the solid phase of cellular structures decreases slightly its Young's modulus and more significantly its strength. Besides, FE simulations with the homogeneous GTN model result in lower stress values compared to experiments. The stress-strain curves of the FE simulations with the heterogeneous GTN model are in good agreement with experiments, exploiting the experimental initial microporosity distribution. Note that these results are obtained with the unique set of plastic and damage parameters of Table 7 and 8 respectively, for the 3 types of models (J2 plasticity, homogeneous GTN and heterogeneous GTN).

The measured values of Young's modulus, compressive yield strength and ultimate compressive strength of the thin-strut and thick-strut samples are detailed in Table 9. The thick-strut sample presents a higher solid (AlSi10Mg) volume fraction which increases its mechanical properties compared to the thin-strut sample. It can be concluded that Young's modulus, compressive yield strength and ultimate compressive strength of the FCC structure increase with

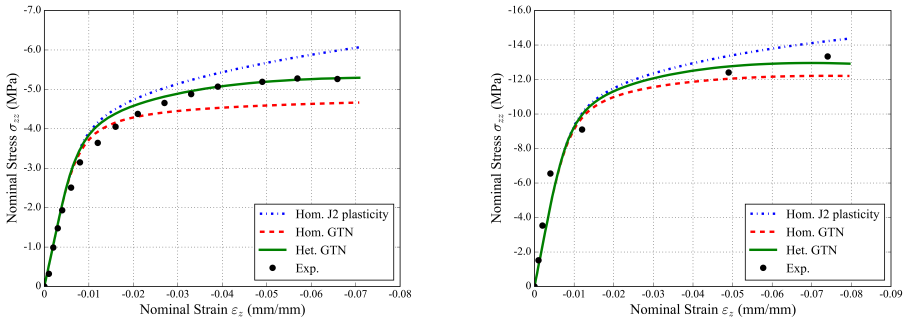


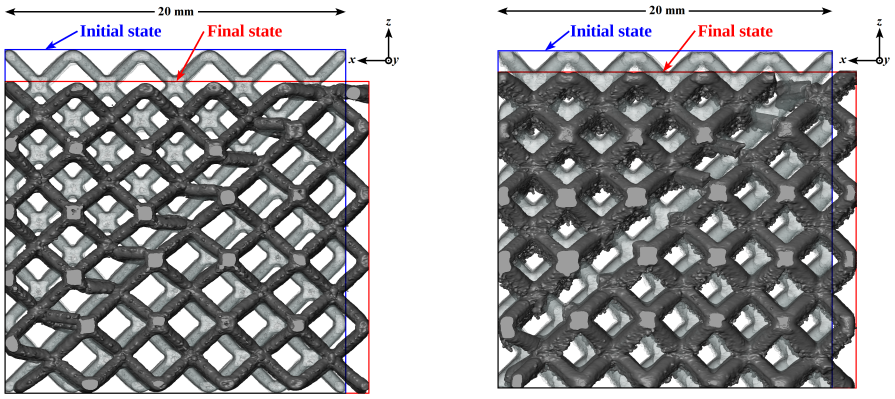
Figure 9: Stress-strain curves obtained by in-situ/ex-situ compression, FE simulations of the (a) thin-strut and (b) thick-strut samples. The dotted blue, dashed red and solid green lines correspond to FE simulations with non porous J2 plasticity, homogeneous GTN and heterogeneous GTN models, respectively.

increasing thicknesses of nodes and struts. This conclusion is consistent with former studies discussing the effect of the volume fraction of solid phase [62, 63] and average struts thickness [64] on the mechanical properties of an open-cell cellular structure. The plastic collapse strain of the thin-strut samples was measured as 0.066 and that of the thick-strut sample as 0.074 .

Table 9: Measured mechanical properties of the thin-strut and thick-strut samples.

Morphology	Young's modulus (GPa)	Compressive yield strength (MPa)	Ultimate compressive strength (MPa)
Thin-strut	0.49	3.2	5.3
Thick-strut	1.77	7.2	13.3

Figures 10(a) and (b) illustrate the initial and fractured states of the thin-strut and thick-strut samples observed by X-ray tomography scanning during the compression tests. The fracture path of both samples occurs on diagonal ($\{101\}$ type) planes located at $\sim 45^{\circ}$ to the loading axis. The struts located near the fracture plane broke mainly close to their ends rather than in the middle of the structure. Thus, the deformation and fracture of the samples are governed mainly by a bending mechanism inducing high local stresses in the vicinity of



(a) (b)

Figure 10: The initial (in transparent) and final (in opaque) deformation states of the (a) thin-strut and (b) thick-strut samples.

nodes. Now looking at the FE model results, Figures 11(a) and (b) illustrate the contour plots of von Mises stress obtained with the homogeneous and heterogeneous GTN models of the thin-strut sample. The contours obtained with the heterogeneous model show areas with higher local stresses mostly concentrated at the strut ends, where the sample failed during the experiments. A similar difference was also observed between the contour plots of von Mises stress resulting from the FE simulations of the thick-strut sample (Figures 12(a) and (b)). Figures 11(c) and (d) illustrate the contours of void volume fraction computed with the homogeneous and heterogeneous GTN models of the thin-strut sample. The homogeneous model presents a soft distribution of VVF in the structure, while that of the heterogeneous model results in areas with high local VVF in the vicinity of the nodes. This difference was also observed between the VVF contours obtained with the FE simulations of the thick-strut sample (Figures 12(c) and (d)).

Figures 13(a) and (b) represent the local contour plots of von Mises stress of the thin-strut sample at a nominal engineering strain ε_z=0.065 , as computed with the homogeneous and heterogeneous models respectively. Figure 13(c)

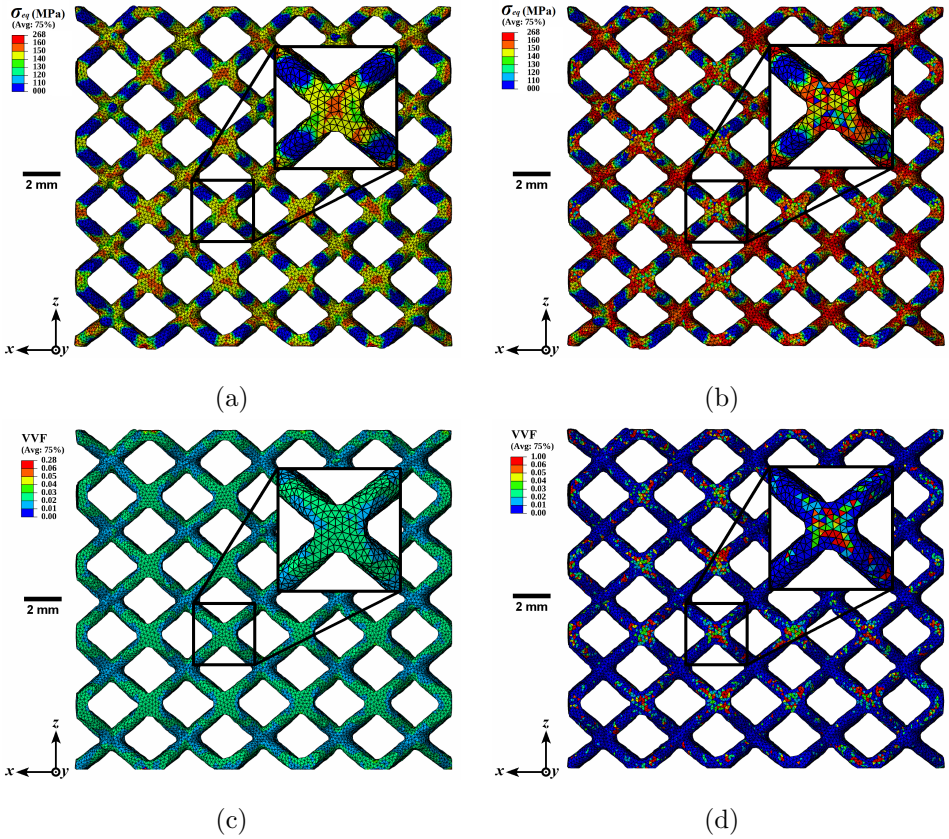


Figure 11: Contour plots of the von Mises stress (a and b) and VVF (c and d) resulting from FE simulations of the homogeneous (a and c) or heterogeneous GTN models (b and d) of the thin-strut sample, at a nominal strain of -0.066 corresponding to experimental plastic collapse strain.

shows the fracture locations observed by X-ray tomography. Figures 13(d) and (e) show the corresponding local contour plots of VVF for the homogeneous and heterogeneous models respectively. The contour plot of von Mises stress of the heterogeneous model shows a higher level of stress concentration than the homogeneous model on the surfaces of the fractured struts. Note that the deformation mechanism in the structure consists mainly in bending, buckling and possibly twisting leading to a non uniform, multiaxial stress state. Therefore, the local stress computed in stress concentration areas of the structure might

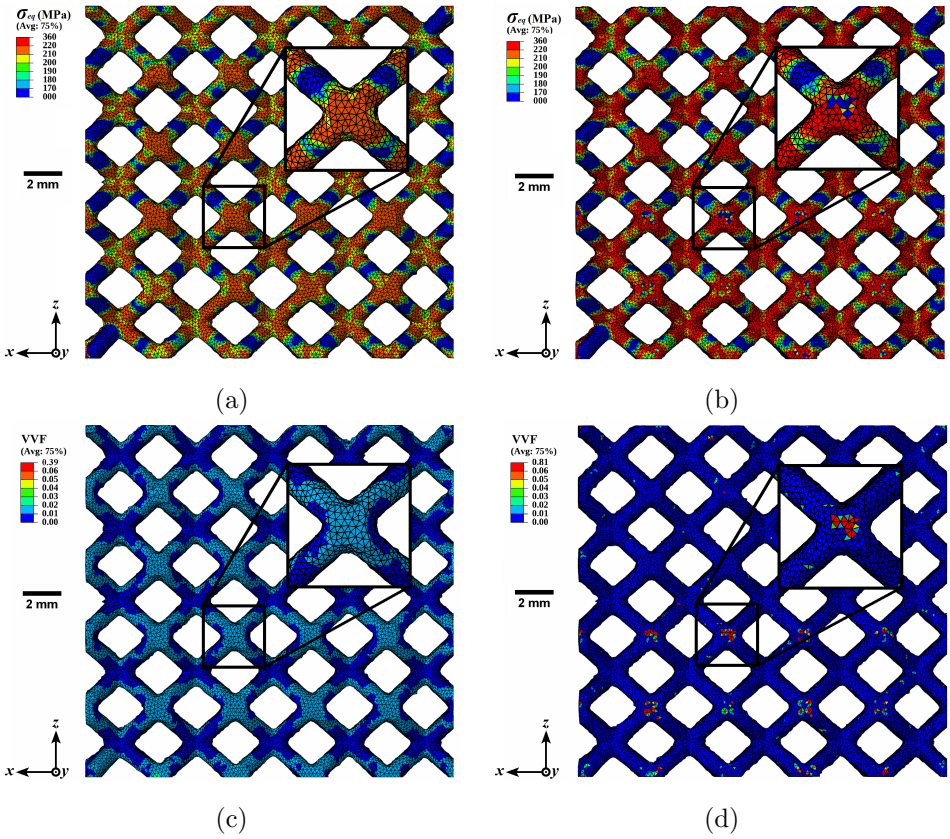


Figure 12: Contour plots of the von Mises stress (a and b) and VVF (c and d) resulting from FE simulations of the homogeneous (a and c) or heterogeneous GTN models (b and d) of the thick-strut sample, at a nominal strain of -0.074 corresponding to experimental plastic collapse strain.

exceed the nominal tensile strength of the bulk material.

The contour plot of the VVF at the strut *external* surface does not allow to anticipate the experimental fracture location, as can be observed in Figure 13(e). As a matter of fact, most of the damage occurs from the *inside* of the struts. This is illustrated in Figures 13(f) and (g), corresponding to the (A-A) and (B-B) cross sections of the fracturing struts, as indicated in Figure 13(e). Despite the von Mises stress being maximum on the surface of the struts, which is coherent with a bending-dominated problem, the VVF is critical in the strut

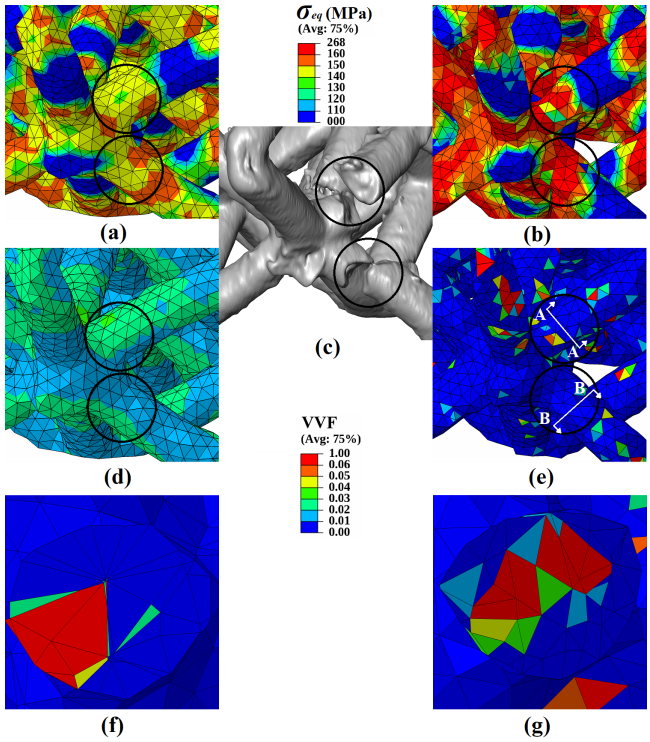


Figure 13: FE contour plots of von Mises stress computed for (a) homogeneous and (b) heterogeneous models. (c) Fracture areas observed by X-ray tomography. FE contour plots of VVF for (d) homogeneous and (e) heterogeneous models. Section view of cutting plane (f) A-A and (g) B-B showing the VVF level for each finite element. All illustrations are produced at a nominal strain of -0.066 corresponding to experimental plastic collapse strain.

interior at fracture locations. This can only be taken into account with the heterogeneous model, allowing to capture the local initial microporosity and its evolution during deformation.

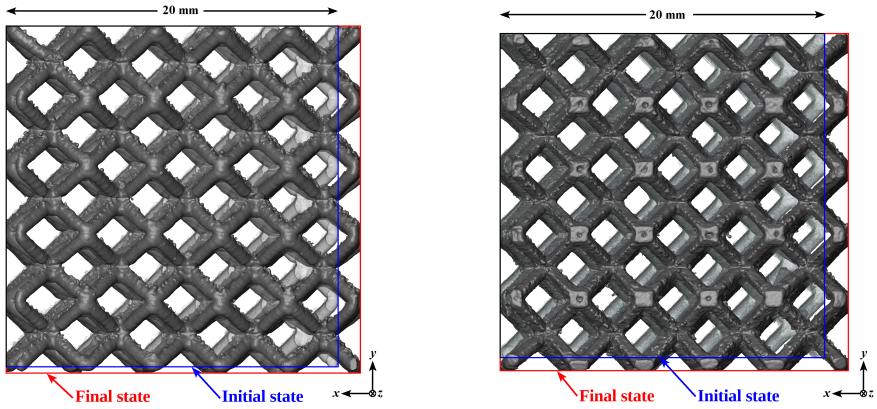
Figures 14(a) and (b) show respectively the elongations of the thin-strut and thick-strut samples in the experimental x and y directions, perpendicular to the compression axis. Figures 15(a) and (b) show the experimentally measured and FE calculated transversal strain values in x and y directions, plotted as a function of the measured axial strain values in z direction. The thin-strut sample is expanding mainly in the x direction. The thick-strut sample is expanding almost

equally in x and y directions. It can be concluded that the strain anisotropy in the transversal directions increases with decreasing node/strut thickness of the sample. However, the transversal strain is always higher in the direction of the lowest node/strut thickness which is x for both thin-strut and thick-strut samples as shown in Figure 5. As illustrated in Figures 15(a) and (b), the model nicely captures the experimental difference in the anisotropy of the two types of samples (thin and thick struts), due to the observed thickness anisotropy in x and y directions.

As a concluding remark, benefiting from the microporosity details in the proposed heterogeneous model allows to better anticipate for potential fracture zones. This is the result of the ability to account for the interaction between a complex local stress state in the structure and the heterogeneous local microporosity. While applied to SLM lattice structures and local microporosity in the present study, the procedure developed here can easily be transfered to other types of structures (e.g. foams or other additively fabricated materials) as well as other types of microstructural details (e.g. local brittle intermetallics fraction in metallic materials). A future development for this study might be to consider a more advanced porous plasticity model (e.g. [65, 66]) allowing to better capture the effective shape of the microcavities inside a given mesh element in contrast to the standard GTN model used in this study, relying on the sole evolution of the (heterogeneous) void volume fraction. Another perspective could be the iterative inverse fitting of the constitutive material parameters based on a comparison between the in situ measured deformation fields and the predicted ones, including image-based boundary conditions to drive the simulations.

5. Conclusions

The present paper focuses on the dual-scale characterization of two FCC structures with thin and thick struts produced by SLM. The initial state of the structure was scanned using the combination of local tomography and double



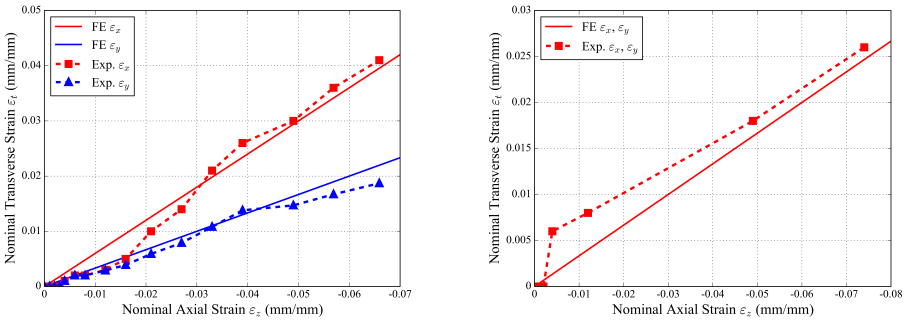
(a) (b)

Figure 14: The initial (transparent) and final (opaque) deformation states of the (a) thin-strut and (b) thick-strut samples in the transversal x and y directions from X-ray tomography scanning.

detector techniques to capture detailed 3D images illustrating both the macroscopic void-cell structure and the local microporosity of the nodes and struts. Deformation of the structures under compression was imaged by in-situ and ex-situ low-resolution X-ray tomography scanning to track the progressive fracture of the samples, to be linked with their initial morphological features. Finally, FE models based on the detailed 3D images were built for the simulation of the compression tests, accounting for the presence of the microcavities. FE calculations taking into account the quantified values of microporosity in each mesh element (called the heterogeneous model) estimated more accurately the fracture location and predicted higher stress concentration near the nodes of the two structures.

Acknowledgment

The authors would like to thank Jérôme Adrien and Joël Lachambre for their help and advises in the use of X-ray tomography. Sirris research centre in Belgium (Lige) provided the SLM samples, Olivier Rigo is particularly



(a) (b)

Figure 15: Nominal transversal strain versus nominal axial strain for (a) thin-strut and (b) thick-strut samples.

acknowledged.

References

[1] L. E. Murr, S. M. Gaytan, D. A. Ramirez, E. Martinez, J. Hernandez, K. N. Amato, P. W. Shindo, F. Medina, R. B. Wicker, Metal fabrication by additive manufacturing using laser and electron beam melting technologies, J. Mater. Sci. Technol. 28 (1) (2012) 1–14. doi:10.1016/S1005-0302(12)60016-4.

[2] K. Kempen, L. Thijs, J. Van Humbeeck, J. P. Kruth, Mechanical properties of AlSi10Mg produced by selective laser melting, Phys. Procedia 39 (2012) 439–446. doi:10.1016/j.phpro.2012.10.059.

[3] K. Hazlehurst, C. J. Wang, M. Stanford, Evaluation of the stiffness characteristics of square pore CoCrMo cellular structures manufactured using laser melting technology for potential orthopaedic applications, Mater. Des. 51 (1) (2013) 949–955. doi:10.1016/j.matdes.2013.05.009.

[4] A. Takaichi, Suyalatu, T. Nakamoto, N. Joko, N. Nomura, Y. Tsutsumi, S. Migita, H. Doi, S. Kurosu, A. Chiba, N. Wakabayashi, I. Yoshimasa, T. Hanawa, Microstructures and mechanical properties of Co-

29Cr-6Mo alloy fabricated by selective laser melting process for dental applications, J. Mech. Behav. Biomed. Mater. 21 (1) (2013) 67–76. doi:10.1016/j.jmbbm.2013.01.021.

[5] I. Rosenthal, A. Stern, N. Frage, Microstructure and mechanical properties of AlSi10Mg parts produced by the laser beam additive manufacturing (AM) technology, Metallogr., Microstruct., Anal. 3 (6) (2014) 448–453. doi:10.1007/s13632-014-0168-y.

[6] P. Delroisse, P. J. Jacques, E. Maire, O. Rigo, A. Simar, Effect of strut orientation on the microstructure heterogeneities in AlSi10Mg lattices processed by selective laser melting, Scr. Mater. 141 (2017) 32–35. doi:10.1016/j.scriptamat.2017.07.020.

[7] A. Elmoutaouakkil, L. Salvo, E. Maire, G. Peix, 2D and 3D characterization of metal foams using X-ray tomography, Adv. Eng. Mater. 4 (10) (2002) 803–807. doi:10.1002/1527-2648(20021014)4:10<803::AID-ADEM803>3.0.CO;2-D.

[8] J. L. C. Rowsell, O. M. Yaghi, Metal–organic frameworks: A new class of porous materials, Microporous Mesoporous Mater. 73 (1-2) (2004) 3–14. doi:10.1016/j.micromeso.2004.03.034.

[9] E. Maire, P. Colombo, J. Adrien, L. Babout, L. Biasetto, Characterization of the morphology of cellular ceramics by 3D image processing of X-ray tomography, J. Eur. Ceram. Soc. 27 (4) (2007) 1973–1981. doi:10.1016/j.jeurceramsoc.2006.05.097.

[10] A. Etiemble, J. Adrien, E. Maire, H. Idrissi, D. Reyter, L. Roué, 3D morphological analysis of copper foams as current collectors for Li-ion batteries by means of X-ray tomography, Mater. Sci. Eng., B 187 (1) (2014) 1–8. doi:10.1016/j.mseb.2014.04.006.

[11] Y. Sun, X. Zhang, Z. Shao, Q. M. Li, Image-based correlation between the

meso-scale structure and deformation of closed-cell foam, Mater. Sci. Eng., A 688 (1) (2017) 27–39. doi:10.1016/j.msea.2017.01.092.

[12] J. A. Elliott, A. H. Windle, J. R. Hobdell, G. Eeckhaut, R. J. Oldman, W. Ludwig, E. Boller, P. Cloetens, J. Baruchel, In-situ deformation of an open-cell flexible polyurethane foam characterised by 3D computed microtomography, J. Mater. Sci. 37 (8) (2002) 1547–1555. doi:10.1023/A:1014920902712.

[13] J. Adrien, E. Maire, N. Gimenez, V. Sauvant-Moynot, Experimental study of the compression behaviour of syntactic foams by in situ X-ray tomography, Acta Mater. 55 (5) (2007) 1667–1679. doi:10.1016/j.actamat.2006.10.027.

[14] S. A. McDonald, G. Dedreuil-Monet, Y. T. Yao, A. Alderson, P. J. Withers, In situ 3D X-ray microtomography study comparing auxetic and non-auxetic polymeric foams under tension, Phys. Status Solidi B 248 (1) (2011) 45–51. doi:10.1002/pssb.201083975.

[15] S. Meille, M. Lombardi, J. Chevalier, L. Montanaro, Mechanical properties of porous ceramics in compression: on the transition between elastic, brittle, and cellular behavior, J. Eur. Ceram. Soc. 32 (15) (2012) 3959–3967. doi:10.1016/j.jeurceramsoc.2012.05.006.

[16] J. Lachambre, E. Maire, J. Adrien, D. Choqueuse, In situ observation of syntactic foams under hydrostatic pressure using X-ray tomography, Acta Mater. 61 (11) (2013) 4035–4043. doi:10.1016/j.actamat.2013.03.017.

[17] C. Petit, E. Maire, S. Meille, J. Adrien, S. Kurosu, A. Chiba, CoCrMo cellular structures made by electron beam melting studied by local tomography and finite element modelling, Mater. Charact. 116 (1) (2016) 48–54. doi:10.1016/j.matchar.2016.04.006.

[18] C. Petit, S. Meille, E. Maire, L. Gremillard, J. Adrien, G. Y. Lau, A. P. Tomsia, Fracture behavior of robocast HA/β-TCP scaffolds studied by X-

ray tomography and finite element modeling, J. Eur. Ceram. Soc. 37 (4) (2017) 1735–1745. doi:10.1016/j.jeurceramsoc.2016.11.035.

[19] S. Youssef, E. Maire, R. Gaertner, Finite element modelling of the actual structure of cellular materials determined by X-ray tomography, Acta Mater. 53 (3) (2005) 719–730. doi:10.1016/j.actamat.2004.10.024.

[20] H. Toda, M. Takata, T. Ohgaki, M. Kobayashi, T. Kobayashi, K. Uesugi, K. Makii, Y. Aruga, 3-d image-based mechanical simulation of aluminium foams: Effects of internal microstructure, Advanced Engineering Materials 8 (6) (2006) 459–467. doi:10.1002/adem.200600035.

[21] D. Lacroix, A. Chateau, M. P. Ginebra, J. A. Planell, Micro-finite element models of bone tissue-engineering scaffolds, Biomaterials 27 (30) (2006) 5326–5334. doi:10.1016/j.biomaterials.2006.06.009.

[22] O. Caty, E. Maire, S. Youssef, R. Bouchet, Modeling the properties of closed-cell cellular materials from tomography images using finite shell elements, Acta Mater. 56 (19) (2008) 5524–5534. doi:10.1016/j.actamat.2008.07.023.

[23] C. Sandino, J. A. Planell, D. Lacroix, A finite element study of mechanical stimuli in scaffolds for bone tissue engineering, J. Biomech. 41 (5) (2008) 1005–1014. doi:10.1016/j.jbiomech.2007.12.011.

[24] I. Jeon, T. Asahina, K. J. Kang, S. Im, T. J. Lu, Finite element simulation of the plastic collapse of closed-cell aluminum foams with X-ray computed tomography, Mech. Mater. 42 (3) (2010) 227–236. doi:10.1016/j.mechmat.2010.01.003.

[25] R. Singh, P. Lee, T. Lindley, C. Kohlhauser, C. Hellmich, M. Bram, T. Imwinkelried, R. Dashwood, Characterization of the deformation behavior of intermediate porosity interconnected ti foams using micro-computed tomography and direct finite element modeling, Acta Biomaterialia 6 (6) (2010) 2342 – 2351. doi:https://doi.org/10.1016/j.actbio.2009.11.032.

[26] C. Veyhl, I. Belova, G. Murch, T. Fiedler, Finite element analysis of the mechanical properties of cellular aluminium based on micro-computed tomography, Materials Science and Engineering: A 528 (13) (2011) 4550 – 4555. doi:https://doi.org/10.1016/j.msea.2011.02.031.

[27] N. Michailidis, Strain rate dependent compression response of ni-foam investigated by experimental and fem simulation methods, Materials Science and Engineering: A 528 (12) (2011) 4204 – 4208. doi:https://doi.org/10.1016/j.msea.2011.02.002.

[28] L. Brabant, J. Vlassenbroeck, Y. d. Witte, V. Cnudde, M. N. Boone, J. Dewanckele, L. van Hoorebeke, Three-dimensional analysis of high-resolution X-ray computed tomography data with Morpho+, Microsc. Microanal. 17 (2) (2011) 252–263. doi:10.1017/S1431927610094389.

[29] L. Zhang, J. M. F. Ferreira, S. Olhero, L. Courtois, T. Zhang, E. Maire, J. C. Rauhe, Modeling the mechanical properties of optimally processed cordierite–mullite–alumina ceramic foams by X-ray computed tomography and finite element analysis, Acta Mater. 60 (10) (2012) 4235–4246. doi:10.1016/j.actamat.2012.04.025.

[30] Y. Hangai, R. Yamaguchi, S. Takahashi, T. Utsunomiya, O. Kuwazuru, N. Yoshikawa, Deformation behavior estimation of aluminum foam by x-ray ct image-based finite element analysis, Metallurgical and Materials Transactions A 44 (4) (2013) 1880–1886.

[31] Y. L. Sun, T. Lowe, S. A. McDonald, Q. M. Li, P. J. Withers, In Situ Investigation and Image-Based Modelling of Aluminium Foam Compression Using Micro X-Ray Computed Tomography, Springer Berlin Heidelberg, Berlin, Heidelberg, 2014, pp. 189–197.

[32] A. Szlancsik, B. Katona, K. Bobor, K. Májlinger, I. N. Orbulov, Compressive behaviour of aluminium matrix syntactic foams reinforced by iron hollow spheres, Mater. Des. 83 (1) (2015) 230–237. doi:10.1016/j.matdes.2015.06.011.

[33] Y. Sun, Q. M. Li, T. Lowe, S. A. McDonald, P. J. Withers, Investigation of strain-rate effect on the compressive behaviour of closed-cell aluminium foam by 3D image-based modelling, Mater. Des. 89 (2016) 215–224. doi:10.1016/j.matdes.2015.09.109.

[34] Y. Chen, R. Das, M. Battley, Finite element analysis of the compressive and shear responses of structural foams using computed tomography, Composite Structures 159 (2017) 784 – 799. doi:https://doi.org/10.1016/j.compstruct.2016.09.091.

[35] C. Petit, E. Maire, S. Meille, J. Adrien, Two-scale study of the fracture of an aluminum foam by X-ray tomography and finite element modeling, Mater. Des. 120 (1) (2017) 117–127. doi:10.1016/j.matdes.2017.02.009.

[36] T. Zhang, E. Maire, J. Adrien, P. R. Onck, L. Salvo, Local tomography study of the fracture of an ERG metal foam, Adv. Eng. Mater. 15 (8) (2013) 767–772. doi:10.1002/adem.201300004.

[37] K. Mangipudi, P. Onck, Multiscale modelling of damage and failure in two-dimensional metallic foams, Journal of the Mechanics and Physics of Solids 59 (7) (2011) 1437 – 1461. doi:https://doi.org/10.1016/j.jmps.2011.02.008.

[38] K. Mangipudi, P. Onck, Notch sensitivity of ductile metallic foams: A computational study, Acta Materialia 59 (19) (2011) 7356 – 7367. doi:https://doi.org/10.1016/j.actamat.2011.07.071.

[39] W. Ronan, V. S. Deshpande, N. A. Fleck, The tensile ductility of cellular solids: The role of imperfections, International Journal of Solids and Structures 102-103 (2016) 200 – 213. doi:https://doi.org/10.1016/j.ijsolstr.2016.10.004.

[40] H. Tankasala, V. Deshpande, N. Fleck, Tensile response of elastoplastic lattices at finite strain, Journal of the Mechanics and Physics of Solids 109 (2017) 307 – 330. doi:https://doi.org/10.1016/j.jmps.2017.02.002.

[41] V. J. Challis, X. Xu, L. C. Zhang, A. P. Roberts, J. F. Grotowski, T. B. Sercombe, High specific strength and stiffness structures produced using selective laser melting, Mater. Des. 63 (2014) 783–788. doi:10.1016/j.matdes.2014.05.064.

[42] B. Gorny, T. Niendorf, J. Lackmann, M. Thoene, T. Troester, H. J. Maier, In situ characterization of the deformation and failure behavior of non-stochastic porous structures processed by selective laser melting, J. Mater. Sci. Eng. A 528 (27) (2011) 7962–7967. doi:10.1016/j.msea.2011.07.026.

[43] R. Mahshid, H. N. Hansen, K. L. Højbjerre, Strength analysis and modeling of cellular lattice structures manufactured using selective laser melting for tooling applications, Mater. Des. 104 (2016) 276–283. doi:10.1016/j.matdes.2016.05.020.

[44] T. Tancogne-Dejean, A. B. Spierings, D. Mohr, Additively-manufactured metallic micro-lattice materials for high specific energy absorption under static and dynamic loading, Acta Mater. 116 (2016) 14–28. doi:10.1016/j.actamat.2016.05.054.

[45] M. R. Karamooz Ravari, M. Kadkhodaei, M. Badrossamay, R. Rezaei, Numerical investigation on mechanical properties of cellular lattice structures fabricated by fused deposition modeling, Int. J. Mech. Sci. 88 (2014) 154–161. doi:10.1016/j.ijmecsci.2014.08.009.

[46] M. Mukherjee, F. García-Moreno, C. Jiménez, A. Rack, J. Banhart, Microporosity in aluminium foams, Acta Materialia 131 (2017) 156–168.

[47] E. Padilla, V. Jakkali, L. Jiang, N. Chawla, Quantifying the effect of porosity on the evolution of deformation and damage in sn-based solder joints by x-ray microtomography and microstructure-based finite element modeling, Acta Materialia 60 (9) (2012) 4017 – 4026. doi:https://doi.org/10.1016/j.actamat.2012.03.048.

[48] M. Kaye, C. Puncreobutr, P. Lee, D. Balint, T. Connolley, D. Farrugia, J. Lin, A new parameter for modelling three-dimensional damage evolution validated by synchrotron tomography, Acta Materialia 61 (20) (2013) 7616 – 7623. doi:https://doi.org/10.1016/j.actamat.2013.08.065.

[49] M. Shakoor, A. Buljac, J. Neggers, F. Hild, T. F. Morgeneyer, L. Helfen, M. Bernacki, P.-O. Bouchard, On the choice of boundary conditions for micromechanical simulations based on 3dimaging, International Journal of Solids and Structures 112 (2017) 83 – 96. doi:https://doi.org/10.1016/j.ijsolstr.2017.02.018.

[50] V. Tvergaard, A. Needleman, Analysis of the cup-cone fracture in a round tensile bar, Acta Metall. 32 (1) (1984) 157–169. doi:10.1016/0001-6160(84)90213-X.

[51] S. Thuillier, E. Maire, M. Brunet, Ductile damage in aluminium alloy thin sheets: Correlation between micro-tomography observations and mechanical modeling, Materials Science and Engineering: A 558 (2012) 217 – 225. doi:https://doi.org/10.1016/j.msea.2012.07.116.

[52] T. Ueda, L. Helfen, T. F. Morgeneyer, In situ laminography study of three-dimensional individual void shape evolution at crack initiation and comparison with gursontvergaardneedleman-type simulations, Acta Materialia 78 (2014) 254 – 270. doi:https://doi.org/10.1016/j.actamat.2014.06.029.

[53] Avizo® 8 user's guide (2014).

[54] J. Schindelin, I. Arganda-Carreras, E. Frise, V. Kaynig, M. Longair, T. Pietzsch, S. Preibisch, C. Rueden, S. Saalfeld, B. Schmid, et al., Fiji: an open-source platform for biological-image analysis, Nat. Methods 9 (7) (2012) 676. doi:10.1186/s12859-017-1934-z.

[55] Y. Amani, A. Takahashi, P. Chantrenne, S. Maruyama, S. Dancette, E. Maire, Thermal conductivity of highly porous metal foams: Experi-

mental and image based finite element analysis, Int. J. Heat Mass Transfer 122 (2018) 1–10. doi:10.1016/j.ijheatmasstransfer.2018.01.050.

[56] J. Y. Buffiere, E. Maire, J. Adrien, J. P. Masse, E. Boller, In situ experiments with X-ray tomography: an attractive tool for experimental mechanics, Exp. Mech. 50 (3) (2010) 289–305. doi:10.1007/s11340-010-9333-7.

[57] A. L. Gurson, Continuum theory of ductile rupture by void nucleation and growth: Part i—yield criteria and flow rules for porous ductile media, J. Eng. Mater. Technol. 99 (1) (1977) 2. doi:10.1115/1.3443401.

[58] C. C. Chu, A. Needleman, Void nucleation effects in biaxially stretched sheets, J. Eng. Mater. Technol. 102 (3) (1980) 249. doi:10.1115/1.3224807.

[59] V. Tvergaard, Influence of voids on shear band instabilities under plane strain conditions, Int. J. Fract. 17 (4) (1981) 389–407. doi:10.1007/BF00036191.

[60] V. Tvergaard, On localization in ductile materials containing spherical voids, Int. J. Fract. 18 (4) (1982) 237–252. doi:10.1007/BF00015686.

[61] Abaqus version 6.13 documentation collection (2013).

[62] T. G. Nieh, K. Higashi, J. Wadsworth, Effect of cell morphology on the compressive properties of open-cell aluminum foams, Mater. Sci. Eng., A 283 (1-2) (2000) 105–110. doi:10.1016/S0921-5093(00)00623-7.

[63] X. Q. Cao, H. Wang, Z, H. W. Ma, L. M. Zhao, G. T. Yang, Effects of cell size on compressive properties of aluminum foam, Trans. Nonferrous Met. Soc. China 16 (2) (2006) 351–356. doi:10.1016/S1003-6326(06)60060-5.

[64] J. Parthasarathy, B. Starly, S. Raman, A. Christensen, Mechanical evaluation of porous titanium (Ti6Al4V) structures with electron beam melting (EBM), J. Mech. Behav. Biomed. Mater. 3 (3) (2010) 249–259. doi:10.1016/j.jmbbm.2009.10.006.

[65] M. Gologanu, J.-B. Leblond, J. Devaux, Approximate models for ductile metals containing non-spherical voidscase of axisymmetric prolate ellipsoidal cavities, Journal of the Mechanics and Physics of Solids 41 (11) (1993) 1723 – 1754. doi:https://doi.org/10.1016/0022-5096(93)90029-F.

[66] T. Pardoen, J. Hutchinson, An extended model for void growth and coalescence, Journal of the Mechanics and Physics of Solids 48 (12) (2000) 2467 – 2512. doi:https://doi.org/10.1016/S0022-5096(00)00019-3.